# Template-free hierarchical trimetallic oxide photocatalyst derived from organically modified ZnCuCo layered double hydroxide

Gholami, Peyman

2022-09-15

Gholami , P , Khataee , A & Ritala , M 2022 , ' Template-free hierarchical trimetallic oxide photocatalyst derived from organically modified ZnCuCo layered double hydroxide ' , Journal of Cleaner Production , vol. 366 , 132761 . https://doi.org/10.1016/j.jclepro.2022.132761

http://hdl.handle.net/10138/350038
https://doi.org/10.1016/j.jclepro.2022.132761

Journal of Cleaner Production 366 (2022) 132761

Contents lists available at ScienceDirect

Journal of Cleaner Production

journal homepage: www.elsevier.com/locate/jclepro

# Template-free hierarchical trimetallic oxide photocatalyst derived from organically modified ZnCuCo layered double hydroxide

Peyman Gholami [a,*], Alireza Khataee [b,c], Mikko Ritala [a,**]

[a] Department of Chemistry, University of Helsinki, P.O. Box 55, Helsinki, 00014, Finland
[b] Research Laboratory of Advanced Water and Wastewater Treatment Processes, Department of Applied Chemistry, University of Tabriz, 51666-16471, Tabriz, Iran
[c] Department of Environmental Engineering, Gebze Technical University, 41400, Gebze, Turkey

ARTICLE INFO

Handling Editor: M.T. Moreira

*Keywords:*
Trimetallic oxide
Dodecylbenzenesulfonate
Hydrogen evolution
Photocatalysis
Antibiotics degradation

ABSTRACT

High-performance photocatalysts have considerable potential to address energy and environmental issues. In this study, dodecylbenzenesulfonate (DBS) modified ZnCuCo layered double hydroxide (DBS-ZnCuCo LDH) microspheres were synthesized through the facile template-free hydrothermal method. Subsequently, ZnCuCo mixed-metal oxides (MMOs) with morphological features of the DBS modified LDH, enhanced surface area, increased light absorption and effective charge separation were prepared by the calcination of the as-synthesized LDH at 650 °C. Structural, morphological, and photoelectrochemical properties of ZnCuCo and DBS-ZnCuCo LDHs and the corresponding MMOs (ZnCuCo MMO1 and ZnCuCo MMO2) were investigated. SEM and TEM images revealed that DBS-ZnCuCo LDH and ZnCuCo MMO2 possess 3D flower-like hierarchical morphologies with interlaced petal-like nanosheets. Although ZnCuCo LDH was inactive for photocatalytic $H_2$ production under visible light irradiation, ZnCuCo MMO2 exhibited a high $H_2$ production rate (3700 μmol $g^{-1}$ $h^{-1}$), benefiting from the synergy of the ZnO, CuO, and $Co_3O_4$. Furthermore, 95% sulfamethazine (SMZ) degradation was obtained after 60 min of photocatalysis, which is considerably higher than the degradation efficiency of ZnCuCo LDH (24%) and ZnCuCo MMO1 (58%). Based on the photoelectrochemical tests, Z-scheme and double charge transfer mechanisms were proposed to explain the enhanced photocatalytic $H_2$ production and degradation of SMZ. Scavenging tests revealed that $O_2^{\bullet-}$ radicals were the main reactive species in the photodegradation of SMZ. A possible degradation pathway was proposed based on the detection of intermediate products.

## 1. Introduction

Climate change and environmental pollution have motivated scientists to conduct extensive studies on the production of clean energy and environmental remediation (Kumar et al., 2021; Mostafa et al., 2022). Increasing energy consumption and consequent environmental concerns in addition to climate change make it essential to seek environmentally friendly and renewable alternative energy sources to fossil fuels. Hydrogen is known as one of the most promising candidates for the future energy supply due to its clean combustion product ($H_2O$) and high gravimetric energy density.

Antibiotics discharged from the effluents of pharmaceutical industries and wastewater treatment plants are the most important emerging aquatic environmental pollutants (Wang et al., 2020b). Most antibiotics are not completely metabolized in humans and animals, and approximately 50–90% of the consumed antibiotics are usually excreted through feces and urine as parent compounds, metabolites, or both (Liu et al., 2020). These compounds are not efficiently removed in traditional wastewater treatment plants owing to their recalcitrance to biological and physico-chemical treatment methods and antibacterial characteristics (Kumar et al., 2021). Therefore, it is necessary to effectively treat aqueous solutions containing antibiotics.

Photocatalysis has shown great potential for $H_2$ evolution and photodegradation of organic contaminants (Kumar et al., 2021). Several studies have investigated the characteristics and state-of-the-art of semiconductors as the core of photocatalytic technologies (Gao et al., 2021; Shen et al., 2020; Zhu et al., 2018). Zinc oxide and titanium dioxide have been extensively used because of their high photocatalytic performance, environmentally friendly nature, stability, and low cost (Li et al., 2020; Liu et al., 2017). In particular, the unique characteristics of

* Corresponding author.
** Corresponding author.
*E-mail addresses:* peyman.gholami@helsinki.fi (P. Gholami), mikko.ritala@helsinki.fi (M. Ritala).

https://doi.org/10.1016/j.jclepro.2022.132761
Received 3 February 2022; Received in revised form 9 June 2022; Accepted 16 June 2022
Available online 19 June 2022

ZnO effectively accelerate the photochemical processes on its surface. Nevertheless, the photocatalytic activity of ZnO is restricted due to its wide band-gap energy (approximately 3.3 eV), limited light absorption, and high recombination rate of photo-induced electron-hole pairs (Li et al., 2020; Zhang et al., 2020). Accordingly, different strategies have been attempted to address these problems, such as heteroatom doping, fabrication of novel heterojunction materials, and designing bi- and trimetallic oxides. Development of bi- and trimetallic oxides containing n-type ZnO and p-type semiconductors (such as CuO and $Co_3O_4$) is a promising method for band-gap engineering and effective separation of photogenerated charge carriers (Li et al., 2020; Zhang et al., 2020). However, trimetallic oxides fabricated by just physically mixing the precursors followed by thermal treatment do not possess a strong contact between the components as needed for effective charge transportation (Yang et al., 2019; Zhu et al., 2018).

Layered double hydroxides (LDHs) can be utilized as precursors for photoactive mixed metal oxides (MMOs) with high surface area and porosity for various applications (Mostafa et al., 2022; Zhang et al., 2021). LDHs are a class of layered materials that consist of positively charged layers and interlayers of exchangeable anions which balance the charge. They are generally expressed by the formula $[M^{2+}_{1-x}M^{3+}_{x}(OH)_2](A^{n-})_{x/n}\cdot mH_2O$, where $M^{2+}$ and $M^{3+}$ are divalent and trivalent metal cations and $A^{n-}$ is an interlayer anion (Mostafa et al., 2022). Intercalation of anionic surfactants with long alkyl chains into the LDH interlayer galleries can enlarge the interlayers distance, resulting in enhancement of morphological and textural properties of LDH.

To the best of our knowledge, there is no report on the fabrication of ZnCuCo trimetallic oxide microspheres for photocatalytic applications. The novelty of this study is in (i) incorporation of dodecylbenzenesulfonate (DBS) into the interlayer galleries of ZnCuCo LDH as a regulator for the growth of interconnected LDH nanolayers and an expander of the interlayer space, and (ii) preparation of flower-like hierarchical ZnCuCo MMO with increased surface area and morphological features of LDH. ZnCuCo MMOs with superior photocatalytic properties were synthesized by calcination of DBS modified ZnCuCo LDH microspheres. Constructing p-n junctions between ZnO, CuO, and $Co_3O_4$ with a layered structure not only improved harvesting of visible light but also enhanced electron transportation, decreased the rate of electron-hole recombination, and increased the effective contact between the photocatalyst and the pollutant molecules. The synthesis of ZnCuCo LDH, DBS-ZnCuCo LDH and corresponding MMOs (ZnCuCo MMO1 and ZnCuCo MMO2) was confirmed with structural, morphological, and photoelectrochemical characterization. $H_2$ production and photodegradation of sulfamethazine (SMZ) were studied using the as-synthesized photocatalysts.

## 2. Materials and methods

### 2.1. Reagents

Zinc nitrate hexahydrate ($Zn(NO_3)_2)_2\cdot 6H_2O$, 98%), copper(II) nitrate trihydrate ($Cu(NO_3)_2\cdot 3H_2O$, 99%), cobalt (II) nitrate hexahydrate ($Co(NO_3)_2\cdot 6H_2O$, 99%), benzoquinone ($C_6H_4O_2$, ≥98%), sodium nitrate ($NaNO_3$, 99%), disodium salt of ethylenediaminetetraacetic acid ($Na_2$-EDTA, $Na_2C_{10}H_{14}N_2O_8$, 99%), hydrogen peroxide ($H_2O_2$, 30%), isopropanol ($C_3H_8O$, 99%), and sodium dodecylbenzenesulfonate (SDBS, $NaCH_3(CH_2)_{11}C_6H_4SO_3$, ≥99%) were obtained from Sigma-Aldrich (Germany). Sulfuric acid ($H_2SO_4$, ≥98%(, sodium hydroxide (NaOH, ≥ 98%(, ethanol ($C_2H_5OH$, 99%), and sulfamethazine ($C_{12}H_{14}N_4O_2S$, 99%) were purchased from Merck (Germany). Glacial acetic acid ($CH_3CO_2H$, Analytical Reagent grade, ≥ 99.7%) and urea ($CO(NH_2)_2$, 99.5%) were provided by Fisher Scientific (UK). Acetonitrile ($C_2H_3N$, LCMS grade) and methanol (LCMS grade, $CH_3OH$) were supplied by Honeywell (USA). Fluorine-doped tin dioxide-coated (FTO) glass substrates were purchased from SOLEMS.

### 2.2. Synthesis of materials

The synthesis of ZnCuCo LDH was conducted as follows: 1.25 mmol $Zn(NO_3)_2\cdot 6H_2O$, 0.625 mmol $Cu(NO_3)_2\cdot 3H_2O$, and 1.25 mmol $Co(NO_3)_2\cdot 6H_2O$ were added into 30 mL deionized water. $Co^{2+}$ was oxidized to $Co^{3+}$ by adding $H_2O_2$ solution (0.1 M). $NaNO_3$ (1 mmol) was added to the solution to ensure sufficient concentration of $NO_3^-$ as exchangeable interlayer anions of the well-ordered ZnCuCo LDH phase. The resulting mixture was stirred for 2 h to form a clear solution. Then, 0.2222 g $NH_4F$ and 0.3 g $CO(NH_2)_2$ were added into the above solution and stirred for an additional 30 min. The obtained solution was poured into a 50-mL Teflon-lined stainless steel autoclave, which was maintained at 160 °C for 4 h. The precipitates were washed with deionized water and absolute ethanol three times. DBS-LDH microspheres were synthesized through the same procedure by adding 100 mg SDBS instead of $NaNO_3$. ZnCuCo MMO1 and ZnCuCo MMO2 were prepared via calcination of ZnCuCo LDH and DBS-ZnCuCo LDH in the air for 4 h, respectively. The samples are denoted as MMO-450, MMO-550, MMO-650, and MMO-750 according to the calcination temperature. An identical approach was used to synthesize the binary metal oxides separately by adding Zn or Cu or Co precursors to the reaction mixture.

### 2.3. Characterization

X-ray diffraction (XRD) patterns were collected using a PANalytical X'Pert Pro MPD diffractometer with a Cu Kα X-ray source. Field emission scanning electron microscopy (FE-SEM, Hitachi S-4800, Japan) was used to study the sample morphology. Elemental mapping was performed using energy-dispersive X-ray spectroscopy (EDS, Oxford INCA 350, UK). Fourier transformation infrared (FTIR) spectra were recorded using an ALPHA II spectrometer (Bruker, Germany). Thermogravimetric analysis (TGA) was performed using a Toledo Stare system (Mettler Toledo, Switzerland) equipped with a TGA 850 thermobalance at a temperature range of 25–800 °C with a heating rate of 10 °C/min in air. Textural characteristics were evaluated by the $N_2$ adsorption/desorption analyzer (Micromeritics 3Flex, USA) at 77 K. X-ray photoelectron spectroscopy (XPS) measurements were carried out using a PHI Quantum (Physical Electronics Inc, USA) with an Al Kα X-ray radiation (1486.6 eV) source.

### 2.4. Photoelectrochemical measurements

Photoluminescence (PL) spectra of LDHs and MMOs were recorded using a PerkinElmer LS45 spectrometer (USA). A Shimadzu (UV–2600, Japan) spectrophotometer was used to collect UV–visible absorption spectra. To prepare photocatalyst-coated electrodes, 5 mg of as-synthesized photocatalyst was added to a solution containing 1000 μL of ethanol and 100 μL of Nafion. The resulting suspension was exposed to ultrasonic irradiation for 30 min. Then, 20 μL of the homogeneously dispersed photocatalyst suspension was cast onto the surface of the cleaned FTO substrate slide (1 × 1 cm2) and dried at 40 °C for 24 h. Linear sweep voltammetry (LSV) and transient photocurrent responses were measured using an Autolab PGSTAT20 potentiostat-galvanostat with a three-electrode system. The photocatalyst-coated FTO slide acted as the working electrode, and a cylindrical platinum net (r = 1.5 cm, h = 3.7 cm) and an Ag/AgCl/KCl (3 M) electrode were utilized as the counter and reference electrodes, respectively. LSV curves were recorded with a scan rate of 100 mV/s. Mott-Schottky data were collected at 1000 Hz in the dark. Electrochemical impedance spectra (EIS) were recorded at 200 mV versus the normal hydrogen electrode (vs NHE) with 5.0 mV amplitude in the $Na_2SO_4$ solution (0.5 M).

### 2.5. Photocatalytic $H_2$ evolution test

In a typical photocatalytic test, 30 mg of photocatalyst was dispersed in 100 ml aqueous solution of $Na_2S$ (0.35 M) and $Na_2SO_3$ (0.25 M) with

ultrasonication (1 h). The suspension was sealed in a Pyrex flask and bubbled with nitrogen gas for 30 min to achieve an anaerobic condition. Then, the suspension was irradiated by 40 W Kessil LED lights (λ = 427 nm) with magnetic stirring. A Honeywell MST Satellite PGD 4–20 mA/R detector was used to measure the evolved $H_2$.

### 2.6. Photocatalytic degradation test

The photocatalytic performances of ZnCuCo MMO1-650, and ZnCuCo MMO2-650 microspheres were assessed through the photodegradation of SMZ (0.3–1.5 mM). A certain amount of the as-fabricated photocatalyst was added to 200 mL of SMZ aqueous solution. Before illumination with visible light, the suspension was stirred for 30 min in dark to achieve an adsorption-desorption equilibrium. Then, the SMZ solution was illuminated for 60 min by visible light (λ = 427, 525, and 740 nm) as described in section 2.5. During the illumination, 4 mL of the solution was taken every 10 min and the decrease in the SMZ concentration was determined using a UV–Vis spectrophotometer (Shimadzu UV–2600, Japan). An Agilent Technologies 1260 Infinity II series system with an Agilent Technologies 6120 Quadruple LC/MS detector and a C18 (4.6 × 100 mm, 4 μm) column was used to identify the intermediates produced during the SMZ degradation.

## 3. Results and discussion

### 3.1. Synthesis of ZnCuCo LDHs and MMOs

LDHs were synthesized via the hydrothermal method described in section 2.2. Metal nitrates were dissolved at a stoichiometric ratio of $Zn^{2+}$:$Cu^{2+}$:$Co^{2+}$ of 2:1:2. $Co^{2+}$ was oxidized to $Co^{3+}$ by the addition of $H_2O_2$. $NaNO_3$ was added to ensure that there were sufficient $NO_3^-$ ions for filling the interlayers in the ZnCuCo LDH phase. After ensuring full dissolution, urea and $NH_4F$ were added. $NH_4F$ acts as a structural-mediating agent to promote formation of nanosheets. When the solution was brought to hydrothermal conditions in an autoclave at 160 °C, urea was first hydrolyzed to $NH_4^+$, $CO_2$, and $OH^-$ ($CO(NH_2)_2 + 3H_2O \rightarrow 2NH_4^+ + CO_2\uparrow + 2OH^-$), increasing the pH of the solution. Subsequently, LDH crystals were formed through the hydrolysis and aggregation of the metal ions (Zhu et al., 2019a). Woo et al. (2011) reported that a well-ordered Zn–Co-LDH–$NO_3$ phase cannot be obtained without the addition of an excess amount of $NaNO_3$. They highlighted the important role of excess nitrate ions in the formation of the nitrate form of Zn–Co-LDH. Kostić et al. (2022) also found that $NO_3^-$ anions could be incorporated into the LDH interlayer when $NaNO_3$ and NaOH were used for the precipitation instead of $Na_2CO_3$ and NaOH. According to the literature, organic anions can be directly incorporated into the interlayer galleries of LDH (Lan et al., 2019; Li et al., 2021). In this study, the direct incorporation of the DBS anions into the LDH interlayer galleries allowed the DBS anions to serve as regulators for the growth of interconnected LDH interconnected nanolayers and expanders of the interlayer space. It is worth noting that the number of incorporated DBS anions could be larger than the anion exchange capacity of LDH, which could be due to (1) the intercalation of excess DBS via non-polar interactions with the hydrophobic alkyl groups of exchanged DBS and (2) adsorption of DBS on external LDH surfaces (You et al., 2002). LDHs are converted to MMOs by calcination at temperatures ranging from 450 to 750 °C, which causes the elimination of the interlayer water molecules and DBS anions (Akil et al., 2022). The flower-like morphology of LDH microspheres remained almost unchanged during the transformation to MMOs. Morphological, structural and photoelectrochemical properties of LDHs and MMOs will be discussed in more detail in section 3.2.

### 3.2. Characterization of materials

#### 3.2.1. Morphological and structural characteristics

SEM and TEM were employed to investigate the morphologies of LDHs and MMOs. ZnCuCo LDH consisted of 3D hierarchical microspheres decorated with numerous interconnected nanolayers, which were almost perpendicular to the surface of the microspheres (Figs. S1a and b). The diameter of the microspheres was about 7 μm and the thickness of the nanolayers was about 50 nm. The SEM images of the DBS-modified LDH revealed flower-like microspheres with diameters similar to the nitrate form of the LDH. However, the thickness of the nanolayers decreased to about 20 nm, which may be related to the intercalation of DBS anions (Figs. S1e and f). The morphologies of MMO1-650 (Fig. 1a and b) and MMO2-650 (Fig. 1 e and f) remained almost unchanged when compared to the LDH and DBS-LDH, respectively, after being calcined at 650 °C. Fig. S2 presents the SEM image of ZnCuCo MMO2-650, which reveals the formation of well-ordered microspheres with uniform size and morphology. The EDS maps and spectra show that the LDHs contain oxygen, cobalt, zinc, copper, and carbon (Fig. S1). Although EDS is not an accurate technique to quantify the light elements (e.g., carbon and oxygen), it can still detect these elements and compare their contents and distributions in the samples. The EDS maps demonstrate the homogenous distribution of all the elements in the photocatalysts. TEM images of the LDH (Fig. S3 a and b) further demonstrated the existence of the 3D hierarchical microsphere structure. MMO2-650 exhibited loosely assembled nanosheets over the surface of the microspheres (Fig. S3 c). Accordingly, a highly porous structure was developed.

The XRD patterns of LDH and DBS-LDH are shown in Fig. S4 a. The diffraction peaks of ZnCuCo LDH match well with the characteristic peaks of hydrotalcite (JCPDS No. 15–0087). The first reflection in the LDH pattern was observed at $2\theta = 11.6°$, which is in good agreement with the (003) plane of hydrotalcite with an interlayer distance ($d_{003}$) of 0.76 nm. For DBS-LDH, no peak was observed at this position and the first reflection shifted to $2\theta = 4.1°$, which indicates the successful formation of the DBS-LDH phase. The interlayer distance of DBS-LDH (2.15 nm) was found to be approximately 2.5 times larger than that of LDH, which is in accordance with the previous studies (Lee et al., 2019; Quispe-Dominguez et al., 2019). The unit cell parameters a and c were calculated based on the formulae: $a = 2d_{110}$ and $c = 3d_{003}$ (Table S1). The parameter a is the average distance between two cations while the parameter c is related to the distance between the layers. The calculated lattice parameters a for LDH (3.06 nm) and DBS-LDH (3.03 nm) were consistent with the literature (Ruan et al., 2016). Possible presence of inorganic ions within the interlayer space along with the DBS ions has no effect on the interlayer distance, which is an important benefit of the one-step synthesis procedure in comparison to other methods, like regeneration and anion exchange. The XRD results revealed that the DBS ions were efficiently intercalated between the cationic layers of LDH (Akil et al., 2022; Sakr et al., 2018).

XRD patterns of MMOs (Fig. 2) show the presence of monoclinic CuO (JCPDS No. 48–1548) and spinel $M_xCo_{3-x}O_4$ (M = Zn and Cu; $0 \leq x \leq 1$) phases in all the samples. No crystallized ZnO phase was formed upon calcination of ZnCuCo LDH at 450 °C. Increasing the temperature to 550 °C resulted in the appearance of the ZnO phase (JCPDS No. 01-080-4199). These observations are in line with the previous studies showing that no complete dissolution of Cu and Zn into the $Co_3O_4$ occurs (Goda et al., 2020; Zhou et al., 2018). Further increase of the calcination temperature to 650 °C led to a growth of the intensity of all the reflections and especially those related to the ZnO phase indicating an improvement in the crystallinity of MMO. No considerable difference was observed between the XRD patterns of MMO1-650, MMO2-650, and MMO1-750. d-spacing values of the (311) plane for MMO1-650, MMO2-650, and MMO1-750 were found to be 2.44, 2.44, and 2.45 Å respectively, which are in accordance with the value reported for the spinel $Co_3O_4$ (2.44 Å; JCPDS No. 42–1467). The appearance of the CuO and ZnO peaks at calcination temperatures above 400 °C was similar to that previously reported (Park et al., 2016; Ye et al., 2022). Xiong et al. reported the synthesis of 2D ultrathin ZnO/$Co_3O_4$ nanomesh heterostructures by calcination of ZIF-8/ZIF-67 powder at 400 °C (Xiong et al.,

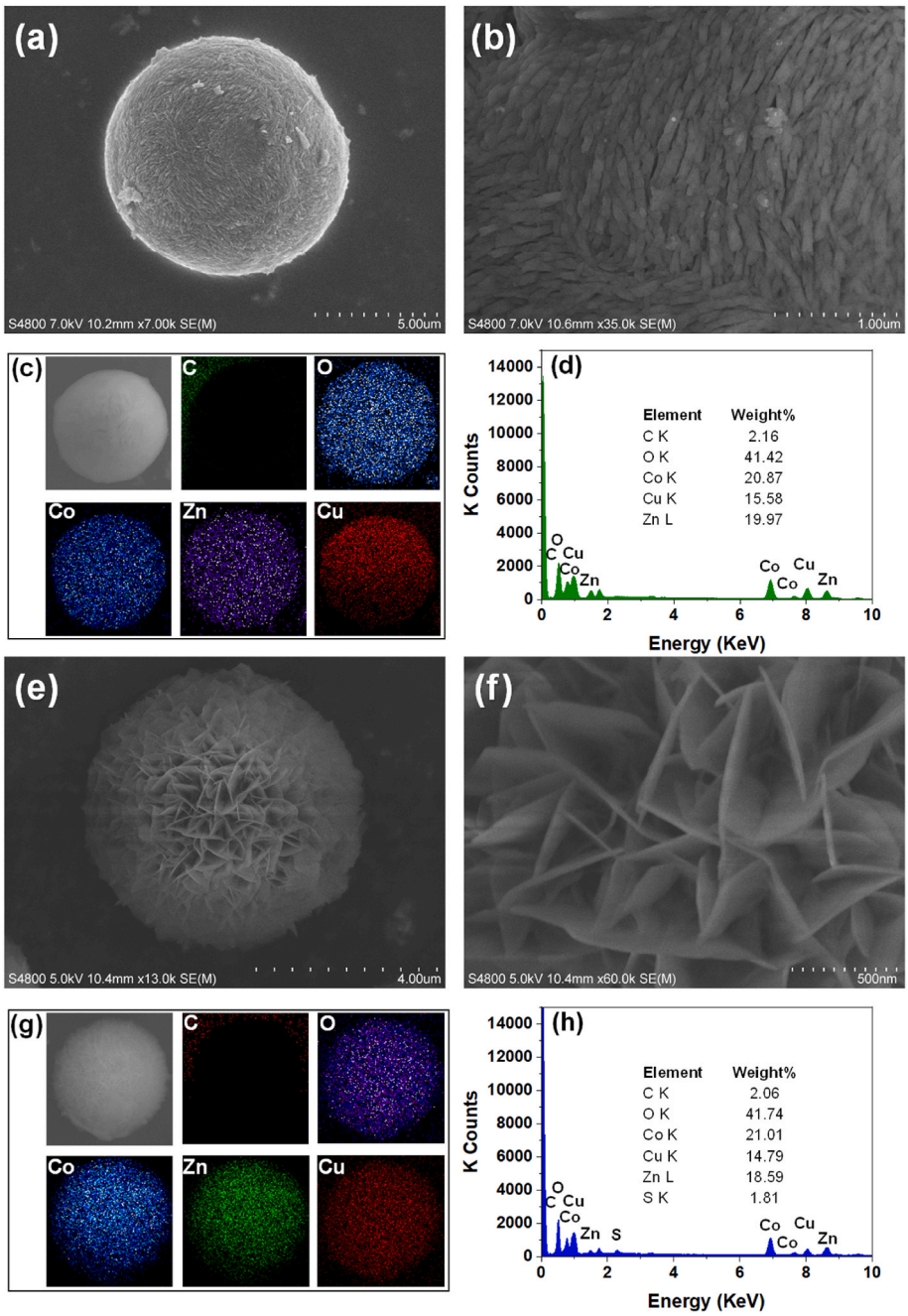


**Fig. 1.** SEM images (a and b), EDS dot mapping (c), and EDS spectra (d) of MMO1-650; SEM images (e and f), EDS dot mapping (g), and EDS spectra (h) of MMO2-650.

2021). Ye et al. also reported the synthesis of hierarchical $Co_3O_4$–NiO hollow dodecahedra by calcination of CoNi-LDH at 450 °C (Ye et al., 2022). Park et al. suggested that the calcination temperature should be maintained below 400 °C to obtain the spinel copper-cobalt oxide structure (Park et al., 2016). However, a part of Zn and Cu could be incorporated into the $Co_3O_4$ structure even upon calcination at 650 °C.

XPS analysis was employed to determine the oxidation states and electronic properties of the different samples. The full XPS spectra of the LDHs and MMOs (Fig. 3a) show the peaks corresponding to C, O, Co, Cu, and Zn. The relative intensity of C 1s in the DBS-LDH spectrum is higher than in the spectrum of LDH, which is related to the presence of DBS in the interlayer galleries of the DBS-LDH. As expected, the carbon content decreases upon calcination of DBS-LDH due to the elimination of DBS. In Fig. 3b, all the photocatalysts exhibit photoelectron signals at 284.7 and 289.4 eV, corresponding to C–C/C=C and O–C=O groups (Zhang et al., 2017). Moreover, a weak peak is observed at 293.3 eV, which can be ascribed to the π-π* satellite (Zhu et al., 2019b).

The carbon residues from the decomposition and combustion of DBS could potentially lead to carbon doping of MMO2 but no signs of this were observed with XPS. According to the literature, the substitution of metal cations by carbon cations would cause an appearance of new peaks in the C 1s high-resolution spectra of ZnO (286.1 eV) (Wang et al., 2014), CuO (289.1 eV) (Wang et al., 2020a), and $Co_3O_4$ (288.4 eV) (Yan et al., 2016). On the other hand, new peaks should appear at lower binding energies (<283 eV) if carbon atoms were in the carbide form, indicating substitution of oxygen by carbon and formation of M–C bonds in the carbon-doped metal oxide structures (Cho et al., 2010; Hosseini et al., 2020). Comparison of the C 1s high-resolution spectra of

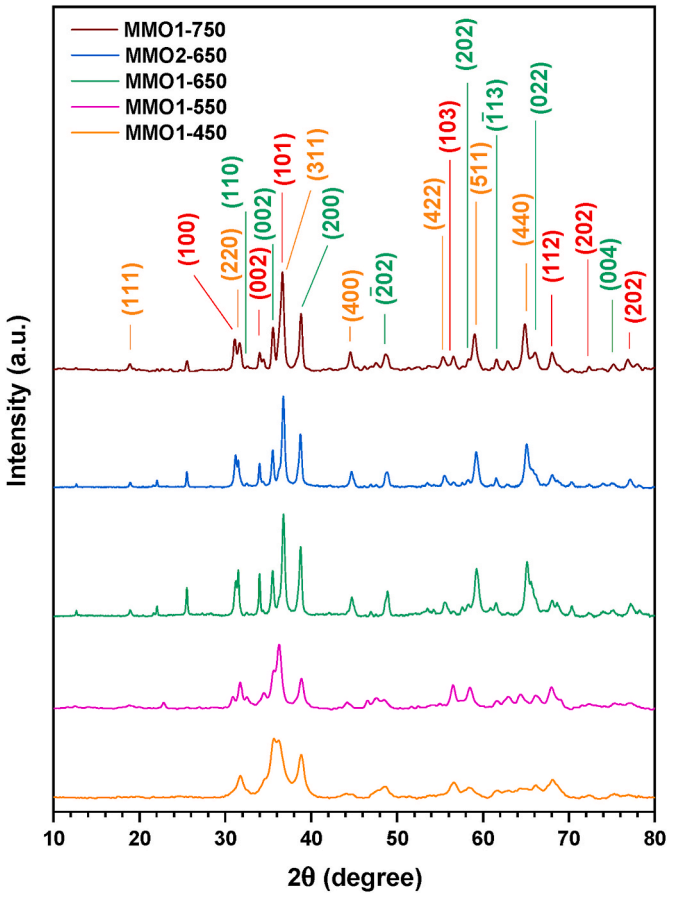


**Fig. 2.** XRD patterns of MMO1-450, MMO1-550, MMO1-650, MMO2-650, and MMO1-750; red, green, and orange colors indicate the lattice planes of ZnO, CuO, and $Co_3O_4$, respectively.

MMO1-650 and MMO2-650 reveals no peaks referring to carbon doping of the oxides despite the incorporation and combustion of DBS in the LDH.

The O 1s high-resolution spectra of LDH and DBS-LDH (Fig. 3c) show that oxygen is present in three forms of M–OH (530.8 eV, M: Zn, Cu, or Co), surface hydroxyl groups, and the coordinatively unsaturated oxygen species (531.4 eV, denoted as $O_S$) and water molecules (532.5 eV) (Chen et al., 2019; Hu et al., 2021). MMO1-650 and MMO2-650 exhibit an additional peak at 529.7 eV, corresponding to the M–O bond in the metal oxides, which confirms the formation of mixed metal oxide upon calcination of LDH (Chen et al., 2019; Tian et al., 2021).

The Zn 2p peak for all the samples is located in the 1021.2–1021.8 eV range, verifying that Zn exists in the oxidation state of $Zn^{2+}$ (Fig. 3d) (Hu et al., 2015; Zhou et al., 2018). The Cu 2p regions illustrate four peaks located in the range of 930–965 eV (Fig. 3e). According to the literature, the Cu $2p_{3/2}$ and Cu $2p_{1/2}$ peaks observed at binding energies of 933.9 and 954.3 eV correspond to $Cu^{2+}$ ions. Both peaks are accompanied by characteristic shake-up satellite peaks that appear in the 938–945 eV and 959–965 eV ranges, which are typical for the oxidation state of +2 (Akil et al., 2022; Hosseini et al., 2020). No peaks assigned to the lower oxidation states of copper were observed in Cu 2p spectra. The Co 2p spectra (Fig. 3f) demonstrate the existence of Co in two oxidation states ($Co^{2+}$ and $Co^{3+}$) by deconvolution of the Co $2p_{3/2}$ and Co $2p_{1/2}$ peaks in the ranges of 777.0–787.0 eV and 794.0–802.0 eV, respectively. The shake-up satellite peaks also demonstrate that cobalt has only two oxidation states of +2 and +3, and there are no other species in the spectrum. For LDH and DBS-LDH, the peaks observed at 781.4 eV and 796.9 eV are ascribed to the $Co^{3+}$ species, while the peaks at 782.8 eV and 797.9 eV are corresponding to the $Co^{2+}$ species (Zhao et al., 2018).

Upon calcination to the MMO, the binding energies of Co $2p_{3/2}$ and Co $2p_{1/2}$ shift to 780.1 eV and 795.2 eV, respectively, revealing the formation of $Co_3O_4$. The decrease in the intensities of satellite peaks further proves the presence of $Co_3O_4$ that was also detected with XRD patterns (Lang et al., 2016). The unmodified LDH and MMO1-650 showed no signs of sulfur whereas the DBS-LDH and MMO2-650 exhibited the S 2p peak around 168.5 eV, which is ascribed to sulfonate and sulfate groups, respectively (Fig. S5).

FTIR analysis was used to identify the functional groups on the unmodified and modified LDH and MMO samples (Fig. 4a). The peaks below 1000 $cm^{-1}$ were attributed to the metal–oxygen (M–O) and metal–oxygen–metal (M–O–M) stretching within the LDH and MMO structures (Ashok et al., 2020; Keyikoglu et al., 2022). The bands located at 1181 and 3370 $cm^{-1}$ belong to the stretching mode of C–N bond and hydroxyl groups, respectively (Orooji et al., 2020; Shi et al., 2020). For DBS-LDH, the bands assigned to the in-plane vibration of C–H (1003 $cm^{-1}$), stretching vibration of the carboxylate group (1438 $cm^{-1}$), C=C (aromatic ring) stretching vibrations (1450-1550 $cm^{-1}$), and the $CH_2$ stretching vibrations (2854 and 2924 $cm^{-1}$) show that DBS anions are incorporated into the LDH interlayer galleries (Hu et al., 2020; Jalili et al., 2020; Khataee et al., 2016; Miao et al., 2020; Rizzo et al., 2010; Valarmathi et al., 2020; Wang et al., 2019a). By comparing the FTIR spectra of DBS-LDH and MMO2-650, the peaks related to the stretching vibrations of the carboxylate group and C=C disappeared upon calcination at 650 °C. Two additional peaks were observed for DBS-LDH and MMO2-650 at 1037 and 1139 $cm^{-1}$ which are attributed to the symmetric and asymmetric stretching vibration of S=O bonds (Patil et al., 2021; Zhao et al., 2020).

The thermal stability of DBS-LDH and MMO2-650 was investigated using thermogravimetry (Fig. 4b). Three steps were observed for the thermal decomposition of DBS-LDH in air. The first step was related to the loss of adsorbed and interlayer water molecules, which occurred at temperatures from 25 to 200 °C. The second step corresponds to the decomposition of DBS which occurred over the temperatures range of 290–430 °C. The third step was attributed to the combustion of residuals of DBS which took place between 580 and 800 °C (Liu et al., 2015). The weight loss related to the removal of DBS from the modified LDH was found to be approximately 20%, which is in good accordance with the results of the EDS analysis. In contrast, MMO2-650 had good thermal stability and a minimal mass loss because water and DBS had been removed already during the calcination at 650 °C.

The $N_2$ adsorption-desorption isotherms of the photocatalysts are shown in Fig. 4c. All the samples show type IV isotherms, revealing mesoporous structures. H3-type hysteresis loops indicate that the photocatalysts may have wedge-shaped pores. Table S2 shows the pore structure parameters for the unmodified and modified LDH and MMO samples. The specific surface area values were determined using the Brunauer-Emmett-Teller (BET) method as 33 and 57 $m^2/g$ for LDH and DBS-LDH, respectively (Table S2). When the LDH samples were calcined to the MMOs, the BET specific surface areas considerably increased to 86 and 179 $m^2/g$ for ZnCuCo MMO1-650 and ZnCuCo MMO2-650, respectively. The increase of the specific surface area was due to the formation of further mesopores in the structures of MMOs by the elimination of volatile species and the combustion of DBS at a high temperature, which also resulted in a growth of the pore volume (Kim et al., 2018). The DBS-modified samples exhibited higher surface areas than the unmodified LDH and MMO. This can be related to the expansion of the interlayer distances by incorporating the larger DBS anions instead of nitrate anions (Deng et al., 2018).This structural feature was maintained even when DBS was removed upon calcination to MMO.

### 3.2.2. Photoelectrochemical properties

A series of optical and electrochemical analyses were performed to acquire further information on the light absorption ability of the photocatalysts and the transfer and separation of photoproduced charge carriers in the photocatalytic processes. Fig. 5a shows the absorption

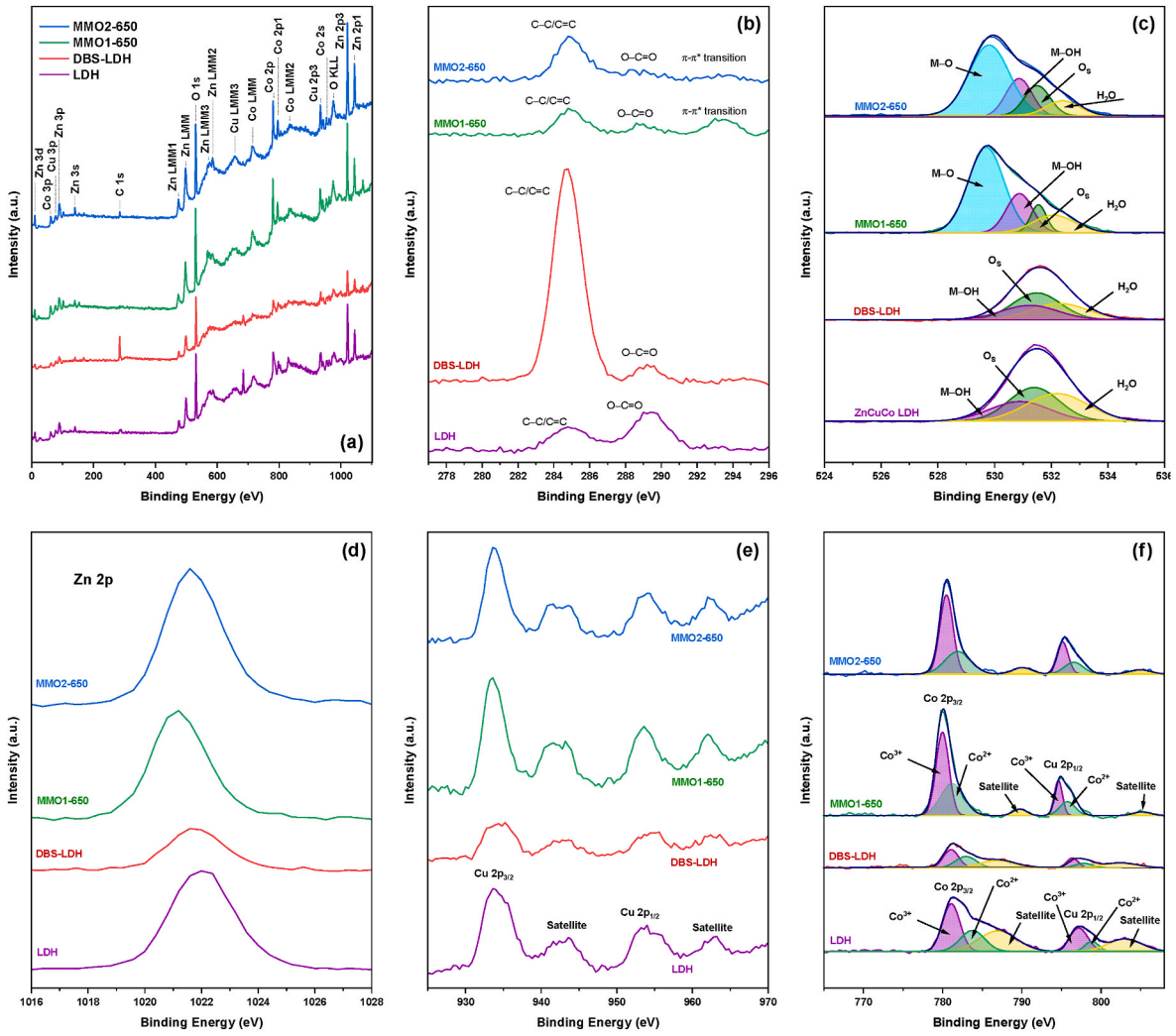


**Fig. 3.** XPS full spectra (a), C 1s (b), O 1s (c), Zn 2p (d), Cu 2p (e), and Co 2p (f) high-resolution spectra of the samples.

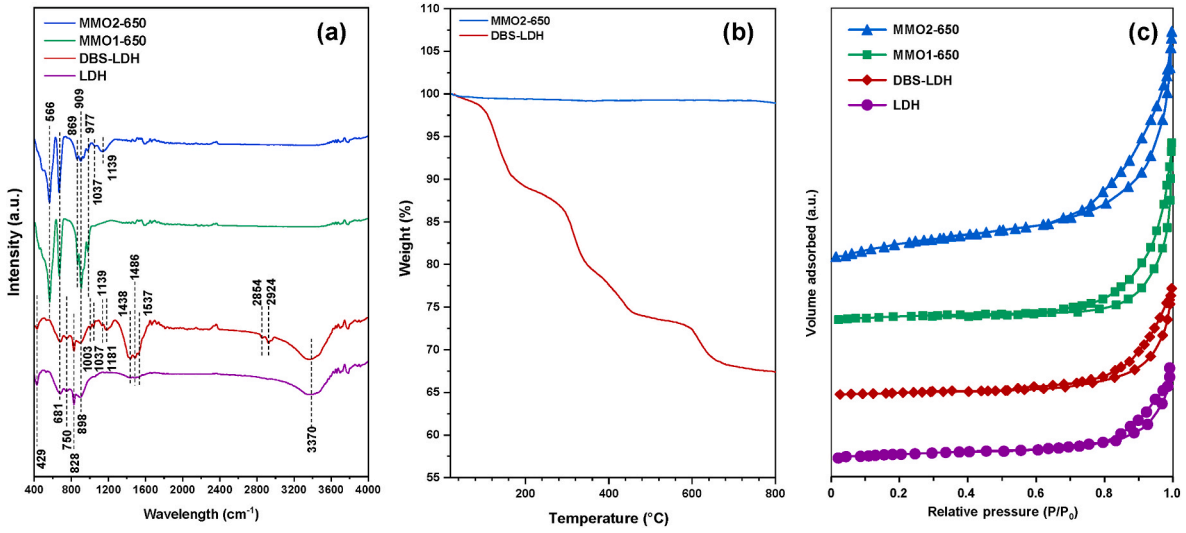


**Fig. 4.** FTIR spectra (a), TGA curves (b), and $N_2$ adsorption-desorption isotherms (c) of the samples.

spectra of the photocatalysts. The absorption edges of LDH and DBS-LDH were observed mostly in the UV region. The calcination of LDHs resulted in a significant change in the optical characteristics of the photocatalysts. The absorption band edges red shifted to the higher wavelength regions (800 nm) after the conversion of LDHs to MMOs. Compared with the LDH samples, MMOs seemed to be superior

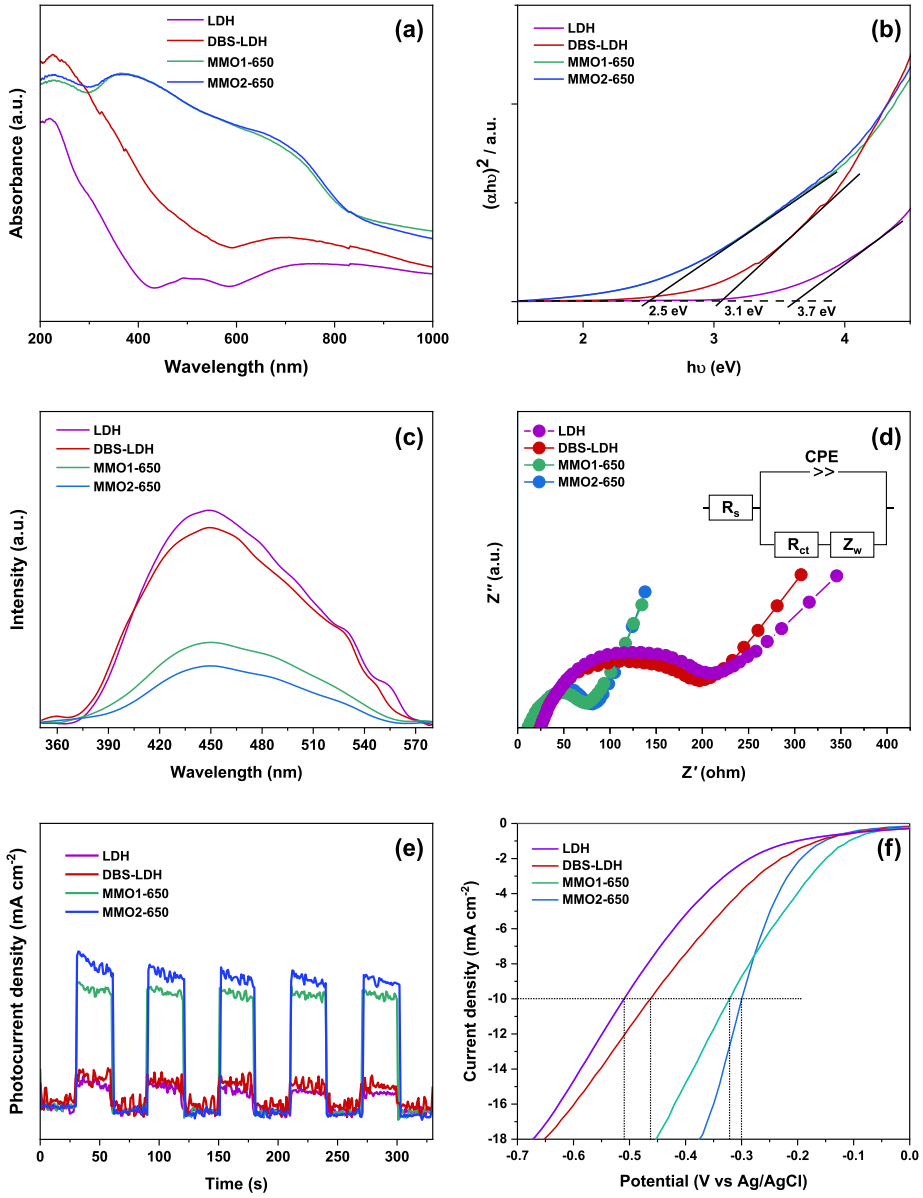


**Fig. 5.** Absorption spectra (a), $(\alpha h\upsilon)^2$-hυ plots (b), PL spectra (c), EIS Nyquist plots (d), transient photocurrent response spectra (e), and LSV curves (f) of the samples.

photocatalysts as they exhibited much higher light absorption abilities in the region from 400 to 800 nm. As seen in Fig. 5b, an $E_g$ of 3.7 eV was evaluated for the LDH using the Tauc plots (Zou et al., 2019). DBS-LDH exhibited a small shift towards lower $E_g$ (about 3.1 eV), which may be due to the charge-transfer transition between DBS and LDH (Hu et al., 2015). The lowest $E_g$ values were observed for the MMO1-650 and MMO2-650 (2.5 eV). After calcination, DBS was completely removed from the interlayer galleries, which explains why both MMOs exhibited similar optical properties. These observations are in good agreement with the EDS and TGA results.

PL spectroscopy can indicate the recombination of photoproduced charges. Decreased PL intensity indicates effective separation of electron-hole pairs. As seen in Fig. 5c, the PL intensities of MMOs are significantly lower than those of LDHs due to the separation of photo-excited charge between ZnO, CuO, and $Co_3O_4$. The mechanism of the transportation and separation of electron-hole pairs will be discussed in more detail in section 3.2.1.

EIS spectra of the samples were recorded to investigate the electron-transfer capacity of LDHs and MMOs. Variations in the electron-transfer ability can be evaluated by detecting changes in the electrochemical impedance. The Nyquist plots (Fig. 5d) of the samples include two main parts: (i) an arc at the high-frequency region, indicating the charge-transfer resistance ($R_{ct}$), and (ii) a linear slope at the low-frequency zone, reflecting the ion-diffusion resistance. A smaller semicircle radius indicates smaller $R_{ct}$ at the charge-transfer zone, increased mobility, and effective separation of the charge carriers. Because the diffusion of charge carriers controls the mass-transfer resistance, a higher line slope indicates lower mass-transfer resistance (Mu et al., 2021). The Nyquist plots were fit to an equivalent circuit displayed in the inset of Fig. 5d, where CPE is the constant-phase element, $Z_w$ is the Warburg impedance, and $R_s$ denotes the total ohmic resistance resulting from the electrolyte resistance, current collector, internal resistance of the electrode, etc. Table S3 represents the $R_s$ and $R_{ct}$ values that were deducted from the first intersecting point and the semicircle diameter, respectively. From Fig. 5d and Table S3, the $R_s$ values of the samples are similar and are in the range 16–27 Ω. However, the $R_{ct}$ values of MMO1-650 and MMO2-650 were almost three times lower than those of LDH and DBS-LDH, which implies higher electric conductivities and

faster electron transfer abilities of the MMOs (Huang et al., 2015; Shen et al., 2020). It is well known that in the LDH structure, metal hydroxides doped with other metal ions have positive charges that are balanced by the anions located between the layers. There are a small number of free electrons available in the LDH structure which results in poor conductivity. In previous studies, the conductivities of LDH materials have been reported to be lower than $10^{-5}$ S $cm^{-1}$ (Huang et al., 2015; Pizzoferrato et al., 2018) After calcination, LDH is transformed into MMO containing ZnO, CuO, and $Co_3O_4$ species, with conductivities in the range of $10^{-2}$ to $10^{-4}$ S $cm^{-1}$ (Huang et al., 2015; Rakshit et al., 2018; Youl Bae and Man Choi, 1999). Accordingly, the enhancement in conductivity can be related to the formation and uniform distribution of ZnO, CuO, and $Co_3O_4$ in MMO (Huang et al., 2015).

The transient photocurrent responses of the LDHs and MMOs to on-off cycles of visible light irradiation at approximately 30-s intervals are presented in Fig. 5e. When the light was turned on, the photocurrent intensity increased quickly and remained constant until the end of the illumination. Then, the current returned as quickly to the low-current density region when the light was turned off. The photocurrent density values of all the samples were reproducible and almost stable during several successive on-off irradiation cycles. The photocurrent responses of MMOs were remarkably higher than those of LDHs, suggesting that in the MMOs the charge carrier recombination phenomenon was more effectively suppressed and the separation of electron-hole pairs improved remarkably.

LSV curves of the materials are shown in Fig. 5f. MMO1-650 and ZnCuCo MMO2-650 show higher current densities than LDH and DBS-LDH, demonstrating more effective electron migration. The potential value generating 10 mA $cm^{-2}$ current density is considered as a vital parameter in evaluation of the electrochemical characteristics of semiconductors (Galani et al., 2020). The corresponding potential values were 0.30, 0.32, 0.47, and 0.51 V (vs Ag/AgCl) for MMO2-650, MMO1-650, DBS-LDH, and LDH, respectively. The depressed performance of LDHs is mainly related to their intrinsic poor charge transfer ability (Yu et al., 2021). The superior performances of MMOs can be ascribed to the synergetic effect of transition metal oxides, which possess narrower bandgap energies, thus improving the electron transfer efficiency (Sun et al., 2019; Wang et al., 2016).

### 3.3. Photocatalytic performance

#### 3.3.1. Photocatalytic hydrogen evolution

Photocatalytic $H_2$ production rates of the as-synthesized photocatalysts were examined under visible light (427 nm) irradiation in the presence of $Na_2S$ and $Na_2SO_3$ as sacrificial reagents. The amount of photocatalyst used was 30 mg in all experiments. No hydrogen was detected in the absence of the photocatalyst or sacrificial reagents under visible light irradiation. The $H_2$ production rates of MMO1-650 and MMO2-650 under 427-nm light irradiation were 2400 and 3700 μmol $g^{-1}$ $h^{-1}$ (Fig. 6a). Based on the results obtained from Mott-Schottky plots (Fig. S6) and the band gap energy values (Fig. S7), the most plausible mechanisms for the improved photocatalytic performance of MMO1-650 and MMO2-650 were suggested. The Mott-Schottky plot of ZnO exhibited a positive slope indicating its n-type nature, whereas CuO and $Co_3O_4$ displayed negative slopes in the Mott-Schottky plots which confirmed their p-type behavior (Fig. S6). As can be observed from the potential-axis intersection points and using the equation $E_{NHE} = E_{Ag/AgCl} + 0.197$ V, the flat-band potentials ($E_{fb}$) of ZnO, CuO, and $Co_3O_4$ were −0.30, 0.81, and 1.02 V (vs NHE), respectively. In general, the $E_{CB}$ of n-type semiconductors is considered to be more negative compared with the $E_{fb}$ by about −0.2 V ($E_{fb}$ – 0.2 V), and the $E_{VB}$ of p-type semiconductors is more positive than $E_{fb}$ by about 0.2 V ($E_{fb}$ + 0.2 V) (Li et al., 2020; Zou et al., 2019). Therefore, the $E_{CB}$ value of ZnO was calculated to be −0.50 V. Similarly, the $E_{VB}$ values of CuO and $Co_3O_4$ were estimated to be 1.00 and 1.22 V, respectively. Considering the $E_g$ values of the as-synthesized semiconductors (Fig. S7), the $E_{VB}$ position of ZnO and $E_{CB}$ positions of CuO and $Co_3O_4$ could be determined ($E_g = E_{VB} - E_{CB}$) as 2.6, −0.9, and −1.38 V, respectively.

Fabrication of the MMO through the calcination of LDH allows close contact between ZnO, CuO, and $Co_3O_4$ with improved interfacial interactions. The light illumination leads to the excitation of electrons from the VB of ZnO, CuO, and $Co_3O_4$ into their CBs and the consequent formation of electron-rich zones in the CBs and the hole-rich zones in the VBs. Considering the determined band-edge energies, Z-scheme transfer (Fig. 7a) and double-charge transfer (Fig. 7b) mechanisms are proposed for the photocatalytic hydrogen evolution using MMO2-650. In the Z-scheme mechanism, the holes and electrons with better oxidation and reduction abilities are preserved by the electron transfer from CB of ZnO to the VBs of CuO and $Co_3O_4$. In contrast, double charge transfer would include electron migration from the higher CBs to a relatively lower CB and hole migration from the lower VBs to a relatively higher VB. Eventually, the accumulated electrons in the CB of CuO and $Co_3O_4$ react with $H^+$ to generate $H_2$. Simultaneously, the photoproduced holes migrate to the surface of the photocatalyst to react with the sacrificial agents ($SO_3^{2-}$ and $S^{2-}$) in the solution (Huang et al., 2015). Regardless of which mechanism dominates, the combination of ZnO, CuO, and $Co_3O_4$ not only improves the light-harvesting ability but also introduces additional active sites and inhibits the recombination of charge carriers (Wang et al., 2019b; Yaghoot-Nezhad et al., 2020). MMO2-650 exhibited a higher hydrogen production rate than MMO1-650, which can be ascribed to the higher specific surface area, the porous structure originating from the expanded interlayer distance in DBS-LDH, and the decomposition of DBS during calcination at 650 °C (Deng et al., 2018; Tao et al., 2018). The stability of MMO1-650 and MMO2-650 catalysts was examined via five consecutive cycles for 30 h. Only a minor decrease (<7%) in $H_2$ production performance was observed over the five cycles (Fig. 6b). To further explore the stability of the MMOs, the XRD patterns were also analyzed after cycling (Fig. S8). No remarkable change occurred in the crystalline structure compared to the fresh photocatalysts; hence, the MMOs are reusable for the $H_2$ production reaction.

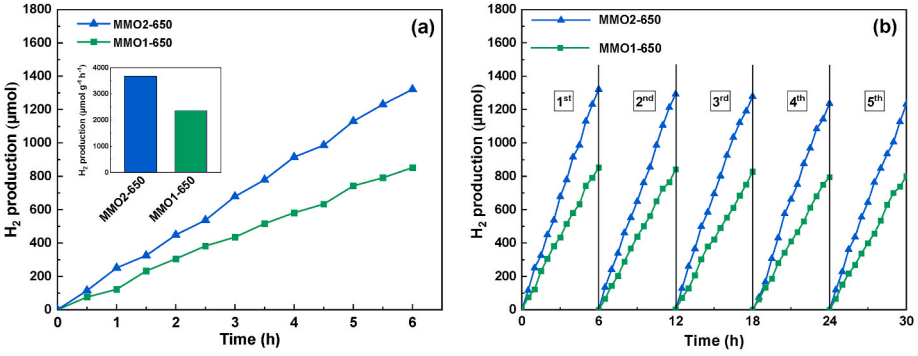


**Fig. 6.** Time course of $H_2$ production and corresponding rate comparison (a) and cyclic stability (b) of MMO1-650 and MMO2-650; photocatalyst amount = 30 mg.

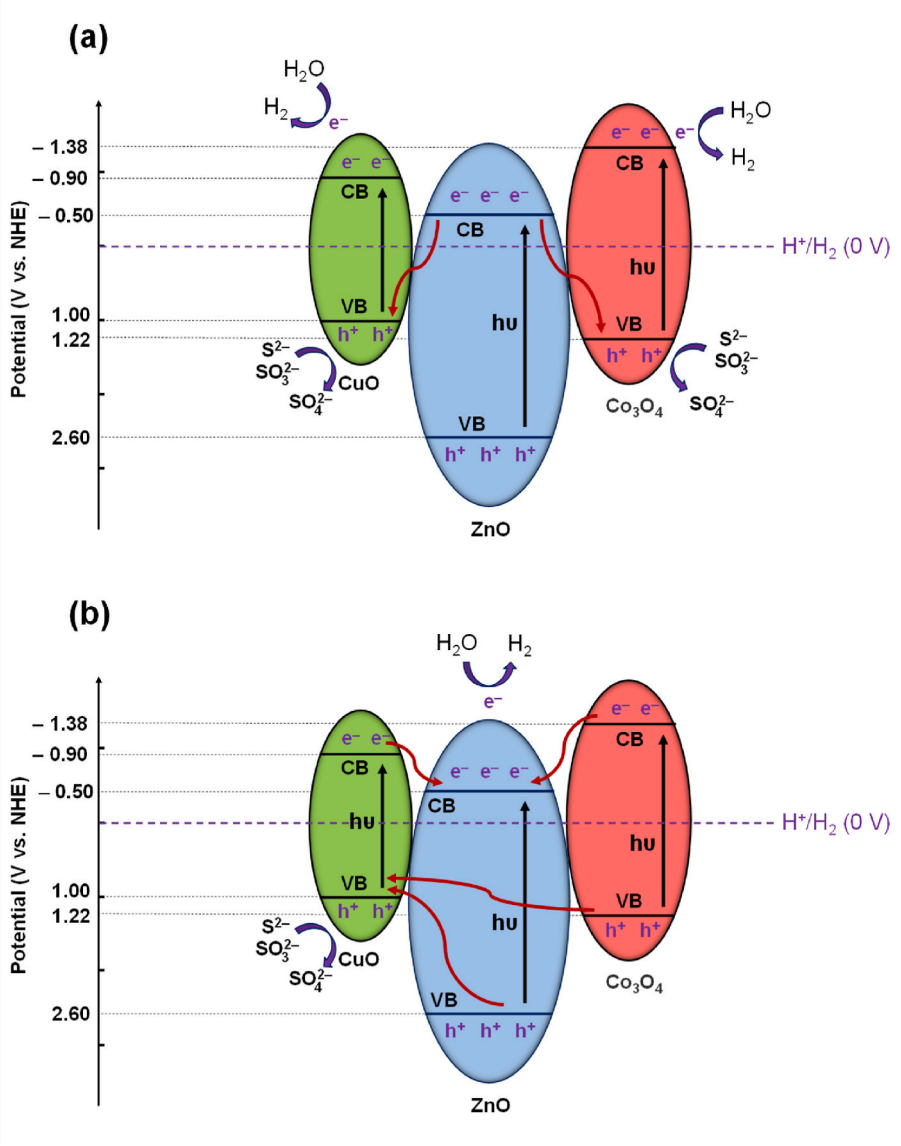


**Fig. 7.** Z-scheme transfer (a) and double charge transfer (b) mechanisms for photocatalytic hydrogen production using MMO2-650.

Table S4 compares the photocatalytic performances and stabilities of MMO2-650 and similar semiconductors reported in previous studies for $H_2$ evolution. The presented comparison reveals that the hierarchical trimetallic oxide microspheres synthesized in this work possess superior photocatalytic performance and reusability when compared with the previously investigated nanostructures.

### 3.3.2. *Photocatalytic degradation of SMZ*

SMZ was selected as the target contaminant to investigate the photocatalytic activity of as-synthesized MMOs. Before illumination, the suspension was stirred for 30 min in dark to reach the adsorption-desorption equilibrium. A small fraction of SMZ molecules (<10%) could be adsorbed on the surface of the photocatalyst during the first 30 min when the suspension was stirred in dark (Fig. 8). Furthermore, only minor degradation (4%) was observed in the absence of photocatalyst under visible light irradiation. The SMZ degradation efficiency was remarkably improved by adding MMO photocatalysts. The photocatalytic degradation of SMZ is based on the excitation of electrons by the absorption of light with photon energy above or equal to the band-gap energy of the photocatalyst. Electrons in the VB are excited and transferred to the CB and hence electron-hole pairs are produced. Then, the photoproduced charge carriers diffuse to the surface of the photocatalyst and react with $H_2O$ or $O_2$ to generate $^{\bullet}OH$ or $O_2^{\bullet-}$ radicals, respectively. After visible light irradiation for 60 min, 58% of SMZ was degraded by MMO1-650. Moreover, 95% degradation efficiency was achieved using MMO2-650, which can be ascribed to its larger surface area that resulted from the DBS modification followed by calcination at 650 °C. By increasing the surface area of the photocatalyst, further active sites are provided for the photocatalytic reactions. Extensive interfaces are introduced between different components of MMOs with a layered structure, which can efficiently improve the migration and separation of photoproduced charge carriers (Gao et al., 2021). Liu et al. (2017) found that sulfate species have a beneficial influence on the photocatalytic performance of Ce-doped $TiO_2$, providing coordinatively unsaturated Lewis acid sites. Surface sulfate groups formed upon the calcination of DBS-LDH can receive electrons from the conduction band and thereby enhance the separation of photoproduced charge carriers and suppress their recombination. Niu et al. (2016) also reported that sulfated Rh–$TiO_2$ photocatalysts showed higher photocatalytic performance in the degradation of Methyl Orange dye when compared to unmodified Rh–$TiO_2$. This improved photocatalytic activity was attributed to the enhanced surface acidity and larger specific surface area.

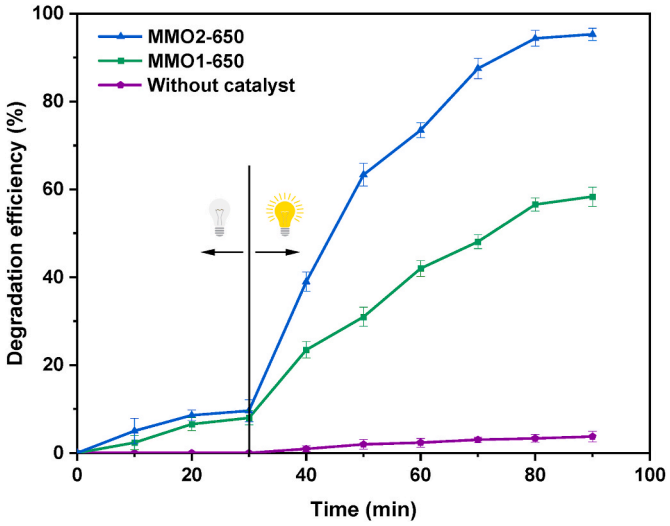


**Fig. 8.** Comparison of the photocatalytic performance of MMO1-650, and MMO2-650 in degradation of SMZ. Experimental conditions: [photocatalyst] = 0.4 g $L^{-1}$, [SMZ] = 0.3 mM and pH = 6.2 (natural pH), photo-excitation wavelength = 427 nm, and irradiation intensity = 352 W $cm^{-2}$.

The reusability of MMO2-650 was evaluated by five successive degradation experiments. After each experiment, the photocatalyst particles were collected by centrifugation, washed with water and dried for reuse. As seen in Fig. S9, no significant decline in SMZ degradation was observed during five cycles. This inferred that MMO2-650 showed excellent reusability in the degradation process.

According to the suggested band gap structure of MMO2-650, the SMZ photodegradation can be explained by the following two mechanisms. In the Z-scheme mechanism (Fig. S10 a), the photoproduced electrons in the CB of ZnO recombine with the photoproduced holes in the VBs of CuO and $Co_3O_4$. Then, the accumulated electrons in the CBs of CuO and $Co_3O_4$ react with $O_2$ to form $O_2^{\bullet-}$ (−0.046 V), and the holes in the VB of ZnO react with $OH^-$ to form $^{\bullet}OH$ (−1.99 V). In the double charge transfer mechanism (Fig. S10 b), the photoproduced electrons in the CBs of CuO and $Co_3O_4$ move to the CB of ZnO. At the same time, the photoproduced holes in the VBs of ZnO and $Co_3O_4$ migrate to the VB of CuO. The electrons moved into the CB of ZnO react with $O_2$ to produce $O_2^{\bullet-}$ and the holes on the VB of CuO react with $OH^-$ to produce $^{\bullet}OH$.

The effects of the main operational parameters, including the amount of MMO2-650, initial SMZ concentration, pH, light wavelength, and irradiation intensity, were investigated on the SMZ photodegradation. The amount of the photocatalyst required is significant for practical and economic considerations. Clearly, increasing the amount of the catalyst from 0.1 to 0.4 g/L led to increased decomposition of SMZ. However, further increase in the amount of MMO2-650 resulted in opacity due to light scattering by the particles and decreased light absorption (Fig. S11 a) (Huang et al., 2019). SMZ degradation declined as its initial concentration increased from 0.3 to 1.5 mM (Fig. S11 b).

The solution pH is also a significant parameter due to the wide pH range of industrial sewage; thus, the effect of pH on the SMZ degradation was studied (Fig. S11 c). The maximum degradation efficiency was observed at pH 6.2. These results could be explained by considering the effect of pH on the charge of the MMO2-650 surface and SMZ. The point of zero charge (PZC) of MMO2-650 was 7.9 as measured by the salt addition method (Sabzroo et al., 2018); hence the photocatalyst was positively charged at pH < 7.9. Furthermore, according to the $pK_a$ values [$pK_{a1}$ = 2.07 (aromatic amine), $pK_{a2}$ = 7.49 (sulfonamide nitrogen)], SMZ exists in its neutral form at pH 6.2 (Zhao et al., 2021). Therefore, there was no repulsive interaction between the SMZ molecules and MMO2-650 at this pH. On the other hand, at higher and lower pH values the compound is predominantly anionic and cationic, respectively, and lower degradation efficiencies were attained in alkaline and acidic conditions because of the repulsive interactions between SMZ and MMO2-650 (Gholami et al., 2019).

The effect of light wavelength on degradation is shown in Fig. S11 d. When the irradiation intensity was kept at 352 W $cm^{-2}$, increasing the wavelength from 427 to 525 and 740 nm led to a 12% and 35% decrease in the degradation efficiency, respectively. This is due to the various levels of photon energy. When photons have higher energy, the electrons excited from the VB gain more energy. Thereby, the probability of reaching the photocatalyst-water interface increases, facilitating the photocatalytic reaction and the separation of charge carriers (Ding and Hu, 2021). Fig. S11 e shows that the SMZ degradation efficiency expectedly decreased with decreasing light intensity. However, even at lower light intensities (down to 88 W $cm^{-2}$), a good SMZ degradation efficiency (69%) was achieved.

Organic scavengers are known to prevent the photogenerated reactive species from reacting with the target pollutant and consequently restrict the degradation efficiency. Hence, scavenging tests were conducted to understand the mechanism of the photocatalytic degradation of SMZ using ZnCuCo MMO2-650 under visible light irradiation. $Na_2$-EDTA, isopropanol (IPA), and 1,4-benzoquinone (BQ) were added to the solution as scavengers of $h^+$, $^{\bullet}OH$, and $O_2^{\bullet-}$, respectively. Changes in the degradation efficiency of SMZ are shown in Fig. S11 f. When $Na_2$-EDTA and IPA were added to the suspension, the degradation of SMZ was slightly inhibited, illustrating that $h^+$ and $^{\bullet}OH$ contribute modestly to the reaction. However, the degradation efficiency decreased from 95% to 33% by adding BQ, indicating that the $O_2^{\bullet-}$ radicals are the main active species in the SMZ degradation process.

### 3.3.3. *Degradation pathway of SMZ*

LC-MS analysis was executed to identify intermediates produced during the photocatalytic degradation of SMZ. Fig. S12 presents the mass spectra of several intermediates in photodegradation using MMO2-650. Although the molecular weight of SMZ (P1) is 278 g $mol^{-1}$, it appears in the protonated form with an m/z of 279 at a retention time of 3.459 min. Based on the detection of eight intermediates with various m/z ratios, a possible degradation pathway is proposed for the SMZ degradation (Fig. 9). The identified compounds indicate that SMZ is decomposed through two main pathways. In the early stages of the process, the reactive species can attack SMZ molecules by hydroxylation of the amine group attached to the benzene ring or by breaking the S–N bond. Regardless of which pathway dominates, the breakage of the S–N bond of SMZ causes the generation of intermediates P2 and P3. Then, P5 is formed by the elimination of $SO_2$ from P2. On the other hand, the oxidation of P3 leads to the formation of P6. Further oxidation of P5 and P6 can result in opening of the benzene and pyrimidine rings, forming aliphatic compounds (such as P7, P8 and P9).

## 4. Conclusions

This work demonstrated the ability of the ZnCuCo LDH host structure to incorporate DBS anions. DBS played a spacer role, enlarging the interlayer distance of the LDH nanolayers with flower-like morphology. LDH was converted to MMO through calcination at 650 °C, providing a close connection between the metal oxides with suitable positions of energy bands. The high surface area (179 $m^2/g$) of the MMO photocatalyst provided extensive contact interfaces between the components for rapid transportation and effective separation of charge carriers for photocatalytic reactions. MMO2-650 exhibited superior textural and optical properties, resulting in enhanced photocatalytic performance in $H_2$ evolution (3700 μmol $g^{-1}$ $h^{-1}$) and SMZ photodegradation (95%). Z-scheme and double charge transfer mechanisms were proposed for the charge carrier transfer in MMO2-650. Less than a 7% decrease in $H_2$ production rate was observed during five consecutive cycles, confirming that the MMO2-650 photocatalyst is reusable and stable. A plausible pathway for SMZ photodegradation was also proposed through the

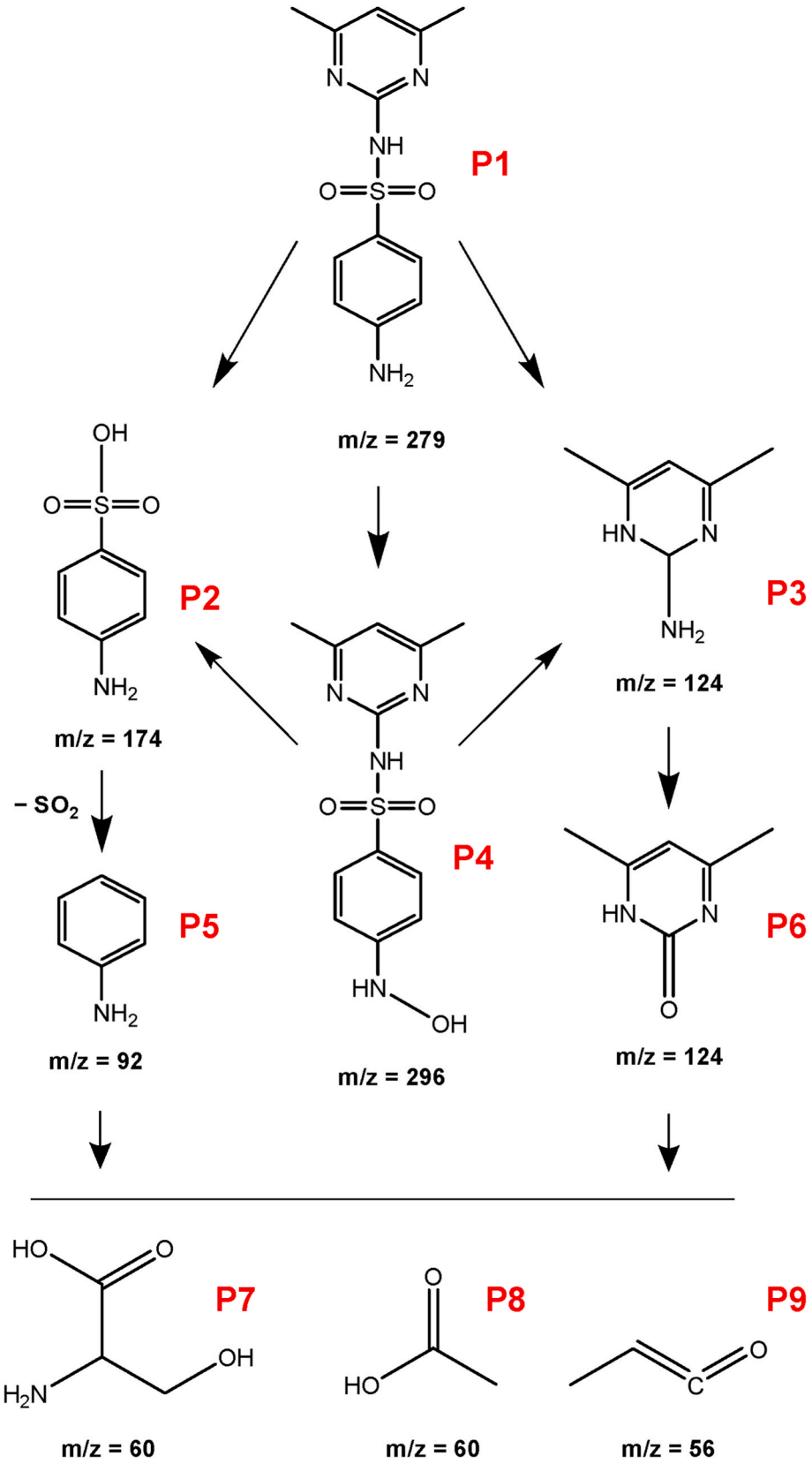


**Fig. 9.** Proposed pathway for SMZ degradation using MMO2-650 photocatalyst.

detection of eight intermediates using LC-MS analysis. The MMO2-650 photocatalyst has considerable potential in $H_2$ production and SMZ degradation.

## CRediT authorship contribution statement

**Peyman Gholami:** Experiments, Writing – original draft, Reviewing and Editing. **Alireza Khataee:** Supervision, Reviewing and Editing. **Mikko Ritala:** Supervision, Resources, Reviewing and Editing.

## Declaration of competing interest

The authors declare that they have no known competing financial interests or personal relationships that could have appeared to influence the work reported in this paper.

## Acknowledgements

The authors acknowledge the financial support provided by the doctoral program in Materials Research and Nanosciences (MATRENA) of the University of Helsinki. XRD analysis, SEM imaging, and EDS measurements were performed using the ALD center Finland research infrastructure.

## Appendix A. Supplementary data

Supplementary data to this article can be found online at https://doi.org/10.1016/j.jclepro.2022.132761.

## References

Akil, J., Ciotonea, C., Siffert, S., Royer, S., Pirault-Roy, L., Cousin, R., Poupin, C., 2022. NO reduction by CO under oxidative conditions over CoCuAl mixed oxides derived from hydrotalcite-like compounds: effect of water. Catal. Today 384–386, 97–105.

Ashok, B., Hariram, N., Siengchin, S., Rajulu, A.V., 2020. Modification of tamarind fruit shell powder with in situ generated copper nanoparticles by single step hydrothermal method. J. Bioresour. Bioprod. 5 (3), 180–185.

Chen, M., Wu, P., Huang, Z., Liu, J., Li, Y., Zhu, N., Dang, Z., Bi, Y., 2019. Environmental application of MgMn-layered double oxide for simultaneous efficient removal of tetracycline and Cd pollution: performance and mechanism. J. Environ. Manag. 246, 164–173.

Cho, S., Jang, J.-W., Lee, J.S., Lee, K.-H., 2010. Carbon-doped ZnO nanostructures synthesized using vitamin C for visible light photocatalysis. CrystEngComm 12 (11), 3929–3935.

Deng, L., Zeng, H., Shi, Z., Zhang, W., Luo, J., 2018. Sodium dodecyl sulfate intercalated and acrylamide anchored layered double hydroxides: a multifunctional adsorbent for highly efficient removal of Congo red. J. Colloid Interface Sci. 521, 172–182.

Ding, H., Hu, J., 2021. Enhancing the degradation of carbamazepine by UVA-LED/$WO_3$ process with peroxydisulfate: effects of light wavelength and water matrix. J. Hazard Mater. 404, 124126.

Galani, S.M., Mondal, A., Srivastava, D.N., Panda, A.B., 2020. Development of $RuO_2$/$CeO_2$ heterostructure as an efficient OER electrocatalyst for alkaline water splitting. Int. J. Hydrogen Energy 45 (37), 18635–18644.

Gao, F., Yuan, J., Huang, X., Lei, R., Jiang, C., Zhuang, J., Liu, P., 2021. Directional transfer of photo-generated charges mediated by cascaded dual defects in ternary photocatalyst ZnS/ZnO-$In_2O_3$ with enhanced photocatalytic performance. Chem. Eng. J. 416, 129159.

Gholami, P., Dinpazhoh, L., Khataee, A., Hassani, A., Bhatnagar, A., 2019. Facile hydrothermal synthesis of novel Fe-Cu layered double hydroxide/biochar nanocomposite with enhanced sonocatalytic activity for degradation of cefazolin sodium. J. Hazard Mater., 120742

Goda, M.N., Said, A.E.-A.A., El-Aal, M.A., 2020. The catalytic performance of ultrasonically prepared $CuxCo_{3-x}O_4$ catalysts towards CO oxidation at relatively low temperature. Mol. Catal. 494, 111121.

Hosseini H, S.M., Siavash Moakhar, R., Soleimani, F., Sadrnezhaad, S.K., Masudy-Panah, S., Katal, R., Seza, A., Ghane, N., Ramakrishna, S., 2020. One-pot microwave synthesis of hierarchical C-doped CuO dandelions/g-$C_3N_4$ nanocomposite with enhanced photostability for photoelectrochemical water splitting. Appl. Surf. Sci. 530, 147271.

Hu, H., Wageh, S., Al-Ghamdi, A.A., Yang, S., Tian, Z., Cheng, B., Ho, W., 2020. NiFe-LDH nanosheet/carbon fiber nanocomposite with enhanced anionic dye adsorption performance. Appl. Surf. Sci. 511, 145570.

Hu, L., Dong, S., Li, Q., Li, Y., Pi, Y., Liu, M., Han, X., Sun, J., 2015. Effects of sodium dodecyl benzene sulfonate on the crystal structures and photocatalytic performance of ZnO powders prepared by hydrothermal method. J. Alloys Compd. 649, 400–408.

Hu, Z., Zhang, D., Sun, C., Song, C., Wang, D., 2021. One-step ionothermal accompanied thermolysis strategy for N-doped carbon quantum dots hybridized NiFe LDH ultrathin nanosheets for electrocatalytic water oxidation. Electrochim. Acta 391, 138932.

Huang, J., Yang, Z., Wang, R., Zhang, Z., Feng, Z., Xie, X., 2015. Zn–Al layered double oxides as high-performance anode materials for zinc-based secondary battery. J. Mater. Chem. 3 (14), 7429–7436.

Huang, S.-M., Weng, C.-H., Tzeng, J.-H., Huang, Y.-Z., Anotai, J., Yen, L.-T., Chang, C.-J., Lin, Y.-T., 2019. Kinetic study and performance comparison of $TiO_2$-mediated visible-light-responsive photocatalysts for the inactivation of Aspergillus Niger. Sci. Total Environ. 692, 975–983.

Jalili, R., Khataee, A., Rashidi, M.-R., Razmjou, A., 2020. Detection of penicillin G residues in milk based on dual-emission carbon dots and molecularly imprinted polymers. Food Chem. 314, 126172.

Keyikoglu, R., Khataee, A., Lin, H., Orooji, Y., 2022. Vanadium (V)-doped ZnFe layered double hydroxide for enhanced sonocatalytic degradation of pymetrozine. Chem. Eng. J. 434, 134730.

Khataee, A., Gholami, P., Vahid, B., 2016. Heterogeneous sono-Fenton-like process using nanostructured pyrite prepared by Ar glow discharge plasma for treatment of a textile dye. Ultrason. Sonochem. 29, 213–225.

Kim, B.-K., Gwak, G.-H., Okada, T., Oh, J.-M., 2018. Effect of particle size and local disorder on specific surface area of layered double hydroxides upon calcination-reconstruction. J. Solid State Chem. 263, 60–64.

Kostić, M., Najdanović, S., Velinov, N., Radović Vučić, M., Petrović, M., Mitrović, J., Bojić, A., 2022. Ultrasound-assisted synthesis of a new material based on MgCoAl-LDH: characterization and optimization of sorption for progressive treatment of water. Environ. Technol. Innovat. 26, 102358.

Kumar, A., Sharma, G., Kumari, A., Guo, C., Naushad, M., Vo, D.-V.N., Iqbal, J., Stadler, F.J., 2021. Construction of dual Z-scheme g-$C_3N_4$/$Bi_4Ti_3O_{12}$/$Bi_4O_5I_2$ heterojunction for visible and solar powered coupled photocatalytic antibiotic degradation and hydrogen production: boosting via $I^-/I_3^-$ and $Bi^{3+}/Bi^{5+}$ redox mediators. Appl. Catal. B Environ. 284, 119808.

Lan, Y., Li, M., Fan, W., Deng, Q., Zeng, Z., Wang, J., Deng, S., 2019. Functional molecules regulated and intercalated nickel-cobalt LDH nano-sheets on carbon fiber cloths as an advanced free-standing electrode for high-performance asymmetric supercapacitors. Electrochim. Acta 321, 134708.

Lang, D., Cheng, F., Xiang, Q., 2016. Enhancement of photocatalytic $H_2$ production activity of CdS nanorods by cobalt-based cocatalyst modification. Catal. Sci. Technol. 6 (16), 6207–6216.

Lee, J.-H., Zhang, W., Ryu, H.-J., Choi, G., Choi, J.Y., Choy, J.-H., 2019. Enhanced thermal stability and mechanical property of EVA nanocomposites upon addition of organo-intercalated LDH nanoparticles. Polymer 177, 274–281.

Li, M., Zhang, S., Li, L., Han, J., Zhu, X., Ge, Q., Wang, H., 2020. Construction of highly active and selective polydopamine modified hollow ZnO/$Co_3O_4$ p-n heterojunction catalyst for photocatalytic $CO_2$ reduction. ACS Sustain. Chem. Eng. 8 (30), 11465–11476.

Li, S.-S., Fang, J.-H., Li, L., Zhu, M., Zhang, F., Zhang, B.-Y., Jiang, T.-J., Zhang, Y.-X., 2021. An ultra-sensitive electrochemical sensor of Ni/Fe-LDH toward nitrobenzene with the assistance of surface functionalization engineering. Talanta 225, 122087.

Liu, J., Zhang, X., Zhang, Y., 2015. Preparation and release behavior of chlorpyrifos adsolubilized into layered zinc hydroxide nitrate intercalated with dodecylbenzenesulfonate. ACS Appl. Mater. Interfaces 7 (21), 11180–11188.

Liu, M., Feng, P., Kakade, A., Yang, L., Chen, G., Yan, X., Ni, H., Liu, P., Kulshreshtha, S., Abomohra, A.E.-F., Li, X., 2020. Reducing residual antibiotic levels in animal feces using intestinal Escherichia coli with surface-displayed erythromycin esterase. J. Hazard Mater. 388, 122032.

Liu, Z., Xing, L., Ma, H., Cheng, L., Liu, J., Yang, J., Zhang, Q., 2017. Sulfated Ce-doped $TiO_2$ as visible light driven photocatalyst: preparation, characterization and promotion effects of Ce doping and sulfation on catalyst performance. Environ. Prog. Sustain. Energy 36 (2), 494–504.

Miao, X., Lin, J., Bian, F., 2020. Utilization of discarded crop straw to produce cellulose nanofibrils and their assemblies. J. Bioresour. Bioprod. 5 (1), 26–36.

Mostafa, M.S., Lan, C., Selim, M.S., Ruiyi, Z., Ya, G., Shuai, Z., Ge, G., 2022. Synthesis of novel CoBiTi LDH and fabrication of LDH-LDO 3D-Heterojunction for enhanced infrared induced water splitting to hydrogen. J. Clean. Prod., 130663

Mu, J., Luo, D., Miao, H., Fan, J., Hu, X., 2021. Synergistic wide spectrum response and directional carrier transportation characteristics of Se/$SnSe_2$/$TiO_2$ multiple heterojunction for efficient photoelectrochemical simultaneous degradation of Cr (VI) and RhB. Appl. Surf. Sci. 542, 148673.

Niu, Y., Li, F., Yang, K., Qiu, T., Wang, R., Lin, C., 2016. Preparation and characterization of sulfated $TiO_2$ with rhodium modification used in esterification reaction and decomposition of methyl orange. Chin. J. Chem. Eng. 24 (6), 767–774.

Orooji, Y., Haddad Irani-nezhad, M., Hassandoost, R., Khataee, A., Rahim Pouran, S., Joo, S.W., 2020. Cerium doped magnetite nanoparticles for highly sensitive detection of metronidazole via chemiluminescence assay. Spectrochim. Acta Mol. Biomol. Spectrosc. 234, 118272.

Park, Y.S., Park, C.S., Kim, C.H., Kim, Y.D., Park, S., Lee, J.H., 2016. Characteristics of the oxygen evolution reaction on synthetic copper-cobalt-oxide electrodes for water electrolysis. J. Kor. Phys. Soc. 69 (7), 1187–1190.

Patil, C.R., Kamble, S.P., Rode, C.V., 2021. Single-pot alcoholysis of furfuryl alcohol to alkyl levulinates using heterogenized p-TSA catalyst. ChemistrySelect 6 (26), 6636–6643.

Pizzoferrato, R., Ciotta, E., Ferrari, I., Braglia, M., Medaglia, P., Mattoccia, A., Di Giamberardino, L., Richetta, M., Knauth, P., Di Vona, M., 2018. Ionic conductivity of ZnAl layered double hydroxide films grown on aluminum substrate. Solid State Ionics 314, 30–35.

Quispe-Dominguez, R., Naseem, S., Leuteritz, A., Kuehnert, I., 2019. Synthesis and characterization of MgAl-DBS LDH/PLA composite by sonication-assisted masterbatch (SAM) melt mixing method. RSC Adv. 9 (2), 658–667.
Rakshit, R., Kadakuntla, S.K., Agarwal, P., Sardar, S., Saha, P., Mandal, K., Rana, D.S., 2018. Surface electronic states induced high terahertz conductivity of $Co_3O_4$ microhollow structure. ACS Appl. Mater. Interfaces 10 (22), 19189–19196.
Rizzo, G., Arena, A., Donato, N., Latino, M., Saitta, G., Bonavita, A., Neri, G., 2010. Flexible, all-organic ammonia sensor based on dodecylbenzene sulfonic acid-doped polyaniline films. Thin Solid Films 518 (23), 7133–7137.
Ruan, X., Chen, Y., Chen, H., Qian, G., Frost, R.L., 2016. Sorption behavior of methyl orange from aqueous solution on organic matter and reduced graphene oxides modified Ni–Cr layered double hydroxides. Chem. Eng. J. 297, 295–303.
Sabzroo, N., Bastami, T.R., Karimi, M., Heidari, T., Agarwal, S., Gupta, V.K., 2018. Synthesis and characterization of magnetic poly(acrylonitrile-co-acrylic acid) nanofibers for dispersive solid phase extraction and pre-concentration of malachite green from water samples. J. Ind. Eng. Chem. 60, 237–249.
Sakr, A.A.E., Zaki, T., Elgabry, O., Ebiad, M.A., El-Sabagh, S.M., Emara, M.M., 2018. Mg-Zn-Al LDH: influence of intercalated anions on $CO_2$ removal from natural gas. Appl. Clay Sci. 160, 263–269.
Shen, J.-C., Zeng, H.-Y., Chen, C.-R., Xu, S., 2020. A facile fabrication of $Ag_2O$-Ag/ZnAl-oxides with enhanced visible-light photocatalytic performance for tetracycline degradation. Appl. Clay Sci. 185, 105413.
Shi, J., Zhang, H., Yu, Y., Yan, M., Liu, L., Zhu, H., Ye, Y., Zhao, Y., Guo, J., 2020. Preparation and adsorption properties of magnetic composite microspheres containing metal–organic double network structure. J. Inorg. Organomet. Polym. Mater. 30 (7), 2301–2314.
Sun, L., Zhuang, Y., Yuan, Y., Zhan, W., Wang, X.-J., Han, X., Zhao, Y., 2019. Nitrogen-doped carbon-coated CuO-$In_2O_3$ p–n heterojunction for remarkable photocatalytic hydrogen evolution. Adv. Energy Mater. 9 (48), 1902839.
Tao, X., Liu, D., Cong, W., Huang, L., 2018. Controllable synthesis of starch-modified ZnMgAl-LDHs for adsorption property improvement. Appl. Surf. Sci. 457, 572–579.
Tian, Y., Huang, A., Wang, Z., Wang, M., Wu, Q., Shen, Y., Zhu, Q., Fu, Y., Wen, M., 2021. Two-dimensional hetero-nanostructured electrocatalyst of Ni/NiFe-layered double oxide for highly efficient hydrogen evolution reaction in alkaline medium. Chem. Eng. J. 426, 131827.
Valarmathi, N., Ameen, F., Almansob, A., Kumar, P., Arunprakash, S., Govarthanan, M., 2020. Utilization of marine seaweed Spyridia filamentosa for silver nanoparticles synthesis and its clinical applications. Mater. Lett. 263, 127244.
Wang, C., Chen, L., Wang, P., Li, M., Liu, D., 2019a. A novel ultrasensitive electrochemiluminescence biosensor for glutathione detection based on poly-L-lysine as co-reactant and graphene-based poly(luminol/aniline) as nanoprobes. Biosens. Bioelectron. 133, 154–159.
Wang, F., Liang, L., Shi, L., Liu, M., Sun, J., 2014. $CO_2$-assisted synthesis of mesoporous carbon/C-doped ZnO composites for enhanced photocatalytic performance under visible light. Dalton Trans. 43 (43), 16441–16449.
Wang, F., Xiao, L., Chen, J., Chen, L., Fang, R., Li, Y., 2020a. Regulating the electronic structure and water adsorption capability by constructing carbon-doped CuO hollow spheres for efficient photocatalytic hydrogen evolution. ChemSusChem 13 (21), 5711–5721.
Wang, H.-F., Tang, C., Zhu, X., Zhang, Q., 2016. A 'point–line–point'hybrid electrocatalyst for bi-functional catalysis of oxygen evolution and reduction reactions. J. Mater. Chem. 4 (9), 3379–3385.
Wang, S., Zhu, B., Liu, M., Zhang, L., Yu, J., Zhou, M., 2019b. Direct Z-scheme ZnO/CdS hierarchical photocatalyst for enhanced photocatalytic $H_2$-production activity. Appl. Catal. B Environ. 243, 19–26.
Wang, Y., Nie, Q., Huang, B., Cheng, H., Wang, L., He, Q., 2020b. Removal of ciprofloxacin as an emerging pollutant: a novel application for bauxite residue reuse. J. Clean. Prod. 253, 120049.
Woo, M.A., Song, M.-S., Kim, T.W., Kim, I.Y., Ju, J.-Y., Lee, Y.S., Kim, S.J., Choy, J.-H., Hwang, S.-J., 2011. Mixed valence Zn–Co-layered double hydroxides and their exfoliated nanosheets with electrode functionality. J. Mater. Chem. 21 (12), 4286–4292.
Xiong, Y., Liu, W., Qiao, X., Song, X., Wang, S., Zhang, X., Wang, X., Tian, J., 2021. Confined synthesis of 2D ultrathin ZnO/$Co_3O_4$ nanomeshes heterostructure for superior triethylamine detection at low temperature. Sensor. Actuator. B Chem. 346, 130486.
Yaghoot-Nezhad, A., Moradi, M., Rostami, M., Danaee, I., Khosravi-Nikou, M.R., 2020. Dual Z-scheme CuO-ZnO@graphitic carbon nitride ternary nanocomposite with improved visible light-induced catalytic activity for ultrasound-assisted photocatalytic desulfurization. Energy Fuels 34 (11), 13588–13605.
Yan, C., Chen, G., Zhou, X., Sun, J., Lv, C., 2016. Template-based engineering of carbon-doped $Co_3O_4$ hollow nanofibers as anode materials for lithium-ion batteries. Adv. Funct. Mater. 26 (9), 1428–1436.
Yang, Y., Cheng, W., Cheng, Y.F., 2019. Preparation of $Co_3O_4$@ZnO core-shell nanocomposites with intrinsic p-n junction as high-performance photoelectrodes for photoelectrochemical cathodic protection under visible light. Appl. Surf. Sci. 476, 815–821.
Ye, J., Cheng, B., Yu, J., Ho, W., Wageh, S., Al-Ghamdi, A.A., 2022. Hierarchical $Co_3O_4$-NiO hollow dodecahedron-supported Pt for room-temperature catalytic formaldehyde decomposition. Chem. Eng. J. 430, 132715.
You, Y., Zhao, H., Vance, G.F., 2002. Hybrid organic–inorganic derivatives of layered double hydroxides and dodecylbenzenesulfonate: preparation and adsorption characteristics. J. Mater. Chem. 12 (4), 907–912.
Youl Bae, H., Man Choi, G., 1999. Electrical and reducing gas sensing properties of ZnO and ZnO–CuO thin films fabricated by spin coating method. Sensor. Actuator. B Chem. 55 (1), 47–54.
Yu, C., Cao, Z., Chen, S., Wang, S., Zhong, H., Ma, X., 2021. In situ selenylation of molybdate ion intercalated Co-Al layered double hydrotalcite for high-performance electrocatalytic oxygen evolution reaction. J. Taiwan Inst. Chem. Eng. 119, 166–176.
Zhang, F., Li, Y.-H., Qi, M.-Y., Tang, Z.-R., Xu, Y.-J., 2020. Boosting the activity and stability of Ag-$Cu_2O$/ZnO nanorods for photocatalytic $CO_2$ reduction. Appl. Catal. B Environ. 268, 118380.
Zhang, N., Huang, Y., Zong, M., Ding, X., Li, S., Wang, M., 2017. Synthesis of ZnS quantum dots and $CoFe_2O_4$ nanoparticles co-loaded with graphene nanosheets as an efficient broad band EM wave absorber. Chem. Eng. J. 308, 214–221.
Zhang, P., Cai, Y., Zhang, L., Mao, Y., Xiang, M., Zhu, Z., Zou, Y., 2021. Superior selective removal of lead via sulfate doped flower like layered double oxide: an example of high value-added utilization of organic waste. J. Clean. Prod. 307, 127267.
Zhao, K., Gao, L., Zhang, Q., Shang, J., 2021. Accumulation of sulfamethazine and ciprofloxacin on grain surface decreases the transport of biochar colloids in saturated porous media. J. Hazard Mater. 417, 125908.
Zhao, W., Ding, H., Zhu, J., Liu, X., Xu, Q., Yin, D., 2020. Esterification of levulinic acid into n-butyl levulinate catalyzed by sulfonic acid-functionalized lignin-montmorillonite complex. J. Bioresour. Bioprod. 5 (4), 291–299.
Zhao, X., Hu, Y., Jiang, H., Yu, J., Jiang, R., Li, C., 2018. Engineering $TiO_2$ supported Pt sub-nanoclusters via introducing variable valence Co ion in high-temperature flame for CO oxidation. Nanoscale 10 (28), 13384–13392.
Zhou, S., Ye, Z., Hu, S., Hao, C., Wang, X., Huang, C., Wu, F., 2018. Designed formation of $Co_3O_4$/$ZnCo_2O_4$/CuO hollow polyhedral nanocages derived from zeolitic imidazolate framework-67 for high-performance supercapacitors. Nanoscale 10 (33), 15771–15781.
Zhu, K., Chen, C., Wang, H., Xie, Y., Wakeel, M., Wahid, A., Zhang, X., 2019a. Gamma-ferric oxide nanoparticles decoration onto porous layered double oxide belts for efficient removal of uranyl. J. Colloid Interface Sci. 535, 265–275.
Zhu, L., Li, H., Xia, P., Liu, Z., Xiong, D., 2018. Hierarchical ZnO decorated with $CeO_2$ nanoparticles as the direct Z-scheme heterojunction for enhanced photocatalytic activity. ACS Appl. Mater. Interfaces 10 (46), 39679–39687.
Zhu, Y., Wang, T., Xu, T., Li, Y., Wang, C., 2019b. Size effect of Pt co-catalyst on photocatalytic efficiency of g-$C_3N_4$ for hydrogen evolution. Appl. Surf. Sci. 464, 36–42.
Zou, Y., Shi, J.-W., Sun, L., Ma, D., Mao, S., Lv, Y., Cheng, Y., 2019. Energy-band-controlled ZnxCd1−xIn2S4 solid solution coupled with g-C3N4 nanosheets as 2D/2D heterostructure toward efficient photocatalytic $H_2$ evolution. Chem. Eng. J. 378, 122192.